

Shaken, and Stirred: Long-Range Dependencies Enable Robust Outlier Detection with PixelCNN++

Barath Mohan U¹, Kushal Chauhan², Pradeep Shenoy², Devarajan Sridharan^{3, 4*}

Abstract

Reliable outlier detection is critical for real-world applications of deep learning models. Likelihoods produced by deep generative models, although extensively studied, have been largely dismissed as being impractical for outlier detection. For one, deep generative model likelihoods are readily biased by low-level input statistics. Second, many recent solutions for correcting these biases are computationally expensive or do not generalize well to complex, natural datasets. Here, we explore outlier detection with a state-of-the-art deep autoregressive model: PixelCNN++. We show that biases in PixelCNN++ likelihoods arise primarily from predictions based on local dependencies. We propose two families of bijective transformations that we term “shaking” and “stirring”, which ameliorate low-level biases and isolate the contribution of long-range dependencies to the PixelCNN++ likelihood. These transformations are computationally inexpensive and readily applied at evaluation time. We evaluate our approaches extensively with five grayscale and six natural image datasets and show that they achieve or exceed state-of-the-art outlier detection performance. In sum, lightweight remedies suffice to achieve robust outlier detection on images with deep generative models.

¹Department of Physics, Indian Institute of Science

²Google Research

³Center for Neuroscience, Indian Institute of Science

⁴Computer Science and Automation, Indian Institute of Science

*Corresponding author: sridhar@iisc.ac.in

Contents

1	Introduction	2	C	De-biasing PixelCNN++ likelihoods: Additional results	10
2	Related Work	2	C.1	Bias in PixelCNN++ likelihoods for grayscale images	10
3	De-biasing PixelCNN++ likelihoods	2	C.2	Comparing PixelCNN++ likelihoods and input complexity (IC): Methods	11
3.1	Components of the PixelCNN++ likelihood	2	C.3	PixelCNN++ ablation experiments: Methods	12
3.2	Global image complexity cannot fully explain the bias in PixelCNN++ likelihoods	3	C.4	Stirring and Shaking: Motivation	13
3.3	Local dependencies strongly bias PixelCNN++ likelihoods	4	C.5	Conditional Correction: Methods	14
3.4	Isolating the contribution of long-range dependencies to PixelCNN++ likelihoods	5	D	Outlier Detection: Additional Results	14
3.5	Bijective transformations for robust outlier detection with PixelCNN++	5	E	Comparison with Competing Approaches	14
	Stirring. • Shaking. • Conditional correction		F	Results without conditional correction	16
4	Experiments	6	G	Alternative Approaches to “Shaking”	17
4.1	Outlier detection performance with stirring and shaking	6	G.1	Varying patch sizes	17
4.2	Comparison with competing methods	7	G.2	Combining shaking and stirring	17
5	Discussion	7	H	Stirring: Subpar performance with EMNIST/MNIST	19
	References	8	I	Shaking: Subpar performance with CIFAR10/LSUN	19
A	Model Architecture and Training	10	J	Reproducibility Checklist	20
B	Datasets and Preprocessing	10			

1. Introduction

Deep discriminative models confidently misclassify test samples that are far removed from their training distributions ([1]). Deep generative models (DGMs), by contrast, offer a potential approach to identify outliers. DGMs model the likelihood distribution of the in-distribution (ID), training data and should, in principle, assign lower likelihoods to unfamiliar, out-of-distribution (OOD) samples. In practice, however, DGMs can assign higher likelihoods to OOD samples, because of biases arising from low-level image statistics [2, 3, 4, 5].

Here, we explore biases in likelihoods produced by a particular, state-of-the-art DGM: PixelCNNs [6]. PixelCNNs are a type of deep autoregressive model that compute the likelihood of an image as a factorized product of the conditional likelihood of its sub-pixels [6]. The likelihood for each pixel is modeled based on the context of preceding sub-pixels using convolutional networks (Fig. 1a-b). We examine the more recent PixelCNN++ model [7]. Despite its ability to produce accurate reconstructions, and generate realistic samples PixelCNN++’s likelihoods are also readily biased, and unreliable for outlier detection [2, 8, 3].

We investigate the origin of the biases in PixelCNN++ likelihoods, and propose effective solutions for correcting for these biases. Our contributions are as follows:

- We show that biases in PixelCNN++ likelihoods arise largely from an over-reliance of the model on local dependencies in the image.
- We devise two efficient solutions based on readily computed bijective transformations of the input samples; these enable correcting for biases arising from local dependencies, and pinpointing the component of the likelihood arising from long-range dependencies.
- The solutions we propose are computationally inexpensive to implement. Moreover, they can be applied *post hoc* during evaluation time, and do not require re-training the model, or training multiple (background) models.
- We evaluate our solutions extensively using 11 inlier (5 grayscale and 6 natural image) datasets and 15 evaluation (7 grayscale and 8 natural image) datasets, and show that they match or exceed state-of-the-art outlier detection performance [2, 8].

2. Related Work

While there is considerable work on outlier detection in supervised settings [9, 10], we focus here, exclusively, on the unsupervised setting where no labels are available. Unlike previous deep, one-class classification approaches [11, 12] we do not employ class label information either for training or for validation.

Perhaps the most relevant approach, for our study is the Input Complexity (IC) metric of [8]. This study characterized an identity relationship between the negative log-likelihood and image complexity, revealing a major source of bias. An elegant outlier detection score was then formulated by simply subtracting image complexity from the negative log-likelihood, with complexity being quantified using the compression length based on standard compressors (e.g. JPEG, PNG, or FLIF). In a later section, we analyze the IC metric and showcase key failure cases that violate the assumptions underlying this approach.

A second relevant study [2], showed that a greater number of zeros in the test image backgrounds biased PixelCNN++ likelihoods toward higher values. This study proposed a training an additional background model, with noise corrupted images, to compute a likelihood ratio that factored out the contribution of background information to the likelihood. In addition to being computationally expensive, due to training multiple models, this metric did not perform well with our (simpler) PixelCNN++ model architecture, as we show subsequently.

Similarly, other approaches involving generative ensembles (e.g. WAIC, [4]) or principled statistical tests (e.g. typicality, [13]) are either computationally expensive or do not perform well with singleton test samples, unlike our approach.

A few studies have examined outlier detection with other classes of generative models like variational autoencoders (VAEs) or flow models. For example, [5] developed a “Likelihood Regret” score for robust outlier detection with VAEs. Yet, this score is expensive to compute because an optimization must be performed by retraining the VAE’s encoder for each sample at test time. Similarly, [14] developed an efficient correction for biases in VAE visible distributions (e.g. Bernoulli) for robust outlier detection. Both of these approaches cannot be readily extended to PixelCNN++ models. Moreover, [15] showed that simple modifications to the architecture of normalizing flows could enable the network to learn semantic features, thereby ameliorating low-level biases. Yet, their modification is specific to flow models, and involves fully retraining the modified model. On the other hand, our approach works with a fully trained model directly, at evaluation time.

3. De-biasing PixelCNN++ likelihoods

3.1 Components of the PixelCNN++ likelihood

To analyze biases in PixelCNN++ likelihoods, we first analyzed the factors that contribute to the likelihood. To model pixel likelihoods PixelCNN++ employs a categorical distribution approximated by a discretized mixture of logistics [7]. Variations in logistic likelihoods can be readily attributed to two sources. One source involves the location parameters (modes) of the underlying mixture of logistics: the model’s best guess of the target pixel value. Accurate prediction of the target pixel value yields a higher log likelihood (Fig. 1c, left). A second source involves the scale parameters (variances)

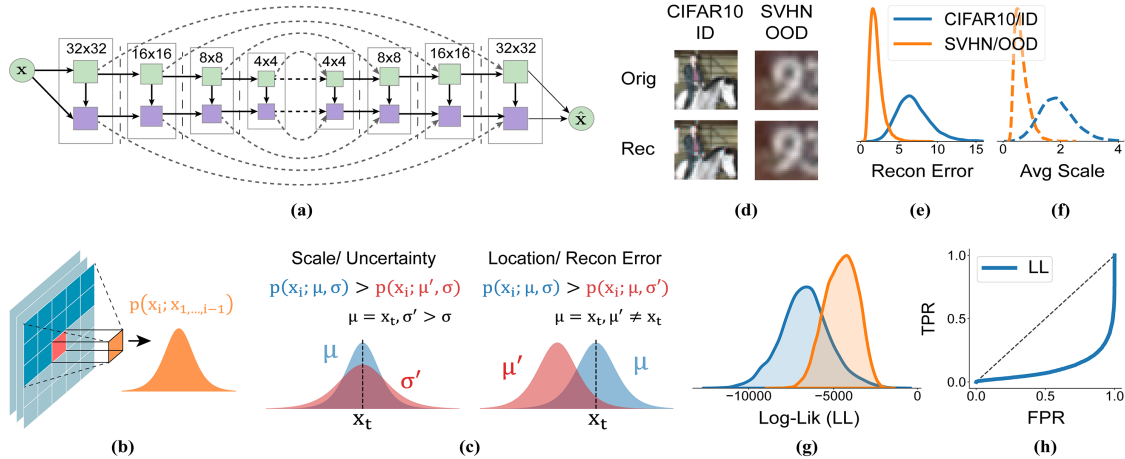


Figure 1. Biases with PixelCNN++ likelihoods. (a) PixelCNN++ model architecture. We use one more hierarchy, including a nested set of 4×4 convolutional layers, as compared the original PixelCNN++ model. Green and purple blocks: vertical and horizontal stacks, respectively. Solid arrows: convolutional connections; curved, dashed arrows: short-cut connections. (b) PixelCNN++ models the likelihood of the current pixel x_i based on the preceding rows and columns of pixels. (c) (Left) Larger the scale of the predicted logistic, higher the uncertainty, and lower the likelihood for the target pixel x_t . (Right) Higher the deviation between the mode of the predicted logistic and x_t , higher the reconstruction error, and lower the likelihood for the target pixel. (d) PixelCNN++ model trained on the CIFAR10 datasets reconstructs both CIFAR10/ID and SVHN/OOD samples well. (e-f) PixelCNN++ reconstruction error (e) and average predicted scale (f) distributions for CIFAR10/ID (blue) and SVHN/OOD (orange) test samples. Surprisingly, SVHN/OOD samples have lower reconstruction error and scale as compared to CIFAR10/ID. (g) PixelCNN++ log likelihood distributions. SVHN/OOD samples get higher log likelihoods as compared to CIFAR10/ID samples. (h) ROC curve for outlier detection using PixelCNN++ likelihoods for CIFAR10/ID and SVHN/OOD. The curve is bowed downwards indicating anomalously higher likelihoods for OOD than ID samples.

of the logistics: the model’s uncertainty with predicting the target pixel. A lower scale parameter (greater certainty) for a mode coinciding with the target pixel value yields higher log likelihoods (Fig. 1c, right). Thus, more accurate predictions (lower reconstruction error) and more confident (less uncertain) predictions of the correct target pixel value, both contribute to higher PixelCNN++ model likelihoods.

We analyzed these two factors for a PixelCNN++ model trained with CIFAR10 images (ID) and tested with SVHN images (OOD) (see Fig. 1d for reconstructions). Remarkably, the model reconstructed OOD samples (Fig. 1e, orange density) with a lower reconstruction error than the ID samples (Fig. 1e, blue density). Moreover, the scale was systematically lower for the OOD samples (Fig. 1f, orange density) than the ID samples (Fig. 1f, blue density) indicating that the model’s predictions were less uncertain with OOD samples. These two factors yielded a higher likelihood values for the SVHN (OOD) images (Fig. 1g, orange density), as compared to the CIFAR10 (ID) images (Fig. 1g, blue density; see Fig. 1h for ROC curve). Similar results were observed also with grayscale data (e.g. MNIST, Appendix C.1). We investigated the reasons behind these trends.

3.2 Global image complexity cannot fully explain the bias in PixelCNN++ likelihoods

A first possibility is that PixelCNN++ likelihoods are systematically biased by the complexity of the image, taken as a whole – a hypothesis previously explored by Serra et al [8].

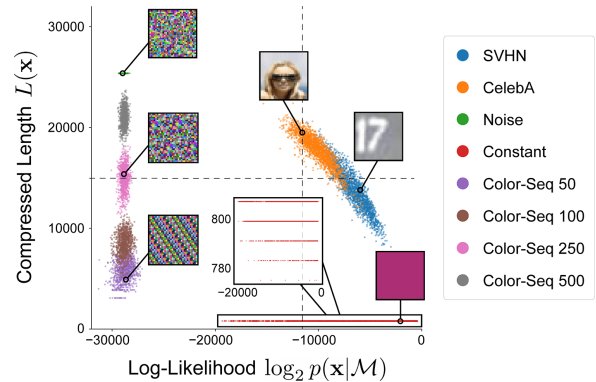


Figure 2. Compressed lengths have a many-to-one relationship with PixelCNN++ likelihood. Compressed length, measured with a PNG compressor, plotted against log-likelihood generated by a PixelCNN++ trained on CIFAR-10 for different OOD datasets (different colors, see text). A wide range of compressed lengths occur for the same model likelihood (dashed vertical line) and vice-versa (dashed vertical line).

Pixel values in less complex images are easier to model because of the stronger spatial correlations among adjacent pixels. Therefore, the comparatively lower complexity of images in datasets like MNIST or SVHN may permit more accurate and more confident predictions of sub-pixel values in these datasets, thereby inflating their likelihoods. Based on this logic, [8] showed that PixelCNN++ negative log likelihoods

exhibit a near-identity relationship with image complexity. They proposed an elegant OOD score that involved simply subtracting the complexity estimate ($L(\mathbf{x})$) from the negative log likelihood (NLL) to account for this “complexity bias”.

To further explore this assumption, we plotted normalized compressed lengths ($L(\mathbf{x})$) using a PNG compressor against log likelihoods ($\log p(\mathbf{x})$) computed with a PixelCNN++ model trained with the CIFAR10 dataset. Although, we observed a strong negative correlation between compressed lengths and log likelihoods for OOD data comprised of natural images, this relationship was systematically violated for certain other kinds of data. Specifically, “constant” images – in which the color across all pixels assumed a constant, uniform value – revealed a nearly flat relationship (Fig. 2, red points). Compressed lengths were virtually identical even as log likelihoods varied over several orders of magnitude ($\log p(\mathbf{x}) = \sim -20000$ to 0) depending on the constant color chosen (Fig. 2, inset). By contrast, images with repeating color sequence patterns across pixels (Appendix C.2) showed the opposite trend – compressed lengths varied over two orders of magnitude ($L(\mathbf{x}) = \sim 250$ to 25000) without a corresponding, substantial change in the log likelihood (Fig. 2, purple, brown, pink, and gray points). In other words, widely different log-likelihoods occurred for images with identical compressed lengths (Fig. 2, dashed horizontal line) and, conversely, images with closely similar log-likelihoods exhibited widely different compressed lengths (Fig. 2, dashed vertical line).

Similar results were observed with other types of compressors (e.g. JPEG, FLIF) and also when considering the “best” compressor (minimum compression length, $L(\mathbf{x}) = \min(L_1(\mathbf{x}), L_2(\mathbf{x}), \dots)$) (Appendix C.2). In other words, the assumption on which the IC metric is predicated – that the compression length provides a reliable estimate of the negative log likelihood under an unbiased, universal model – appears to not hold true across all types of images.

3.3 Local dependencies strongly bias PixelCNN++ likelihoods

An alternative hypothesis for biased likelihoods is that the PixelCNN++ model exploits local dependencies in the dataset to make accurate and confident predictions. For example, both SVHN and MNIST images typically comprise of digits with relatively simple features (as compared to, for example, images of animals), embedded in a fairly uniform background. With knowledge of simple local features like edges and contours the model can accurately predict sub-pixel values even in OOD images, simply by looking within a local neighborhood, and without learning about the long-range structure of the data.

We tested this hypothesis using simple ablations to the PixelCNN++ model (Fig. 3a). In the model, the innermost parts of the network were introduced to capture long-range dependencies over longer spatial scales, a direct consequence of using strided convolutions over progressive layers [7]. In

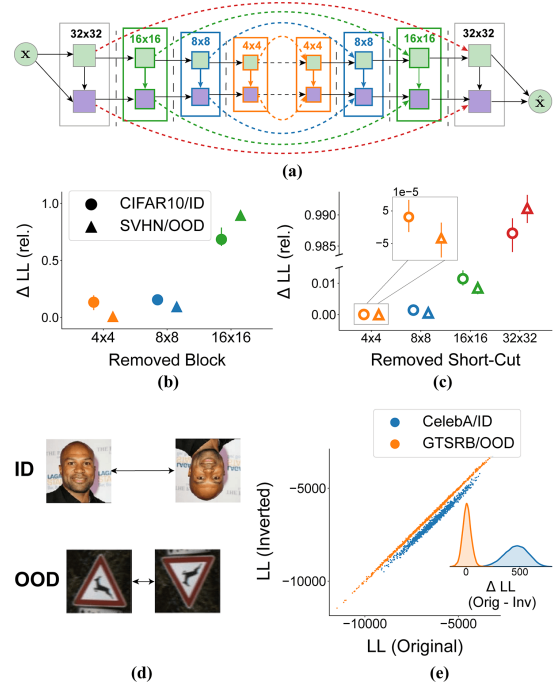


Figure 3. PixelCNN++ relies heavily on local dependencies for prediction. (a) A PixelCNN++ model was trained on CIFAR10/ID and tested on SVHN/OOD. Ablation experiments were performed by removing the outermost (local dependency) or innermost (long-range dependency) blocks. Blocks of matching sizes (e.g. 8×8) were ablated jointly (matching colors). Additional ablations were performed by removing each set of short-cut connections, in-turn. (b) Effect of ablating convolutional blocks on model likelihood. Orange, blue, and green: contribution of the 4×4 , 8×8 , and 16×16 blocks respectively. (c) Effect of ablating short-cut connections on model likelihood. Orange, blue, green and red: contribution of the 4×4 , 8×8 , 16×16 , and 32×32 short-cut connections, respectively. (d). A PixelCNN++ model was trained on CelebA/ID and tested on GTSRB/OOD. We expect log-likelihoods of original and inverted images to more similar for GTSRB/OOD samples than for CelebA/ID samples. (e) Log-likelihoods of the inverted images plotted against their original counterparts, for CelebA/ID and GTSRB/OOD. (Inset) Difference between log likelihoods of original and rotated samples (ΔLL) is higher for CelebA/ID than for GTSRB/OOD.

our PixelCNN++ model, in addition to the 8×8 and 16×16 CNN layers in the standard model, we introduced another sequence of 4×4 layers in the innermost part of the network (Fig. 3a, orange block).

We tested the effect of progressively removing nested hierarchies of the innermost 4×4 , 8×8 and 16×16 convolutional layers on model likelihoods (Appendix C.3). Precisely in line with our hypothesis, removing the 4×4 layers (Fig. 3b, orange triangle) produced virtually no change in the log likelihoods (LLs) for OOD data (SVHN OOD vs CIFAR-10/ID). Nonetheless, successively ablating the 8×8 (Fig. 3b, blue triangle) or

16×16 (Fig. 3b, green triangle) innermost blocks, and especially the latter, produced substantially greater reductions in likelihoods. In other words, the model relied primarily on local dependencies when making predictions with OOD data. By contrast, for ID test data, even just removing the 4×4 block (Fig. 3b, orange circle) produced a noticeable change in the likelihoods, indicating that the model had learned to exploit long-range dependencies when making predictions with ID data. These progressive changes in likelihoods were accompanied by progressively higher reconstruction errors and more uncertain predictions in the model (Appendix C.3). Removing the short-cut connections, at different levels, in turn yielded similar results with the largest reduction in likelihoods occurring when the outermost layer (32×32) connections (Fig. 3c, red symbols) were removed. As before, ablating the innermost layers had a greater effect on likelihoods for ID than for OOD data (Fig. 3c, circles vs triangles).

In sum, the PixelCNN++ model relied strongly on local dependencies for accurate and confident predictions. Yet, removing network components that captured long-range dependencies (innermost layers) produced larger changes in likelihoods for inlier than for outlier samples. We sought to exploit these differences for efficient outlier detection.

3.4 Isolating the contribution of long-range dependencies to PixelCNN++ likelihoods

Given the strong bias in PixelCNN++ likelihoods induced by local dependencies, we explored simple transformations to the input images that would preserve local dependencies, but systematically perturb long-range dependencies. We hypothesized that perturbing long-range (but not local) dependencies would produce a stronger degradation of the likelihood for ID data as compared to OOD data.

To illustrate this idea we explore a transformation by “inversion”. Because the PixelCNN++ model has a specific order of scanning and predicting pixels in the image (upper left to lower right), upon inversion characteristic image features fall into a context that is not familiar to the model. For example, inverting an image of a face positions the eyes below the nose, and the nose below the mouth (Fig. 3d, top). A PixelCNN++ model trained, for example, on a dataset with face images (e.g. CelebA) would then predict pixels in an inverted face image less accurately and with higher uncertainty than pixels in a standard, upright face. As a result, the model would yield lower likelihoods for inverted CelebA images rather than for upright images. We hypothesized that this would not occur for OOD images (e.g. GTSRB). In this case, the model is unlikely to rely on long-range predictions for either the upright or the inverted GTSRB images because both categories of images are equally unfamiliar (Fig. 3d, bottom). Thus, the model should yield equivalent likelihoods for both inverted and upright GTSRB images.

We tested, and confirmed, this hypothesis with the a PixelCNN++ model trained on the CelebA dataset. The model yielded systematically lower likelihoods for inverted faces

than for upright faces in the ID data (Fig. 3e, blue points). In contrast, the model yielded virtually identical likelihoods for OOD (GTSRB) images (Fig. 3e, orange points).

One solution for outlier detection is then to simply subtract the log likelihood of the original image from that of the perturbed (inverted) image to isolate the contribution arising from long-range dependencies. With this reasoning, we propose an “outlier detection score” as follows:

$$\log p_{LR}(\mathbf{x}) = \log p_{\theta}(\mathbf{x}) - \log p_{\theta}(\mathbf{x}')$$

where θ represents the PixelCNN++ model parameters, \mathbf{x} represents the test sample (image, in this case), \mathbf{x}' represents the same test sample after a perturbation that preserves local dependencies but disrupts long-range dependencies, $\log p_{\theta}(\mathbf{x})$ represents the log likelihood of sample yielded by the PixelCNN++ model and $\log p_{LR}$ represents a component of the log likelihood that depends primarily on long-range dependencies in the model. This formulation can also be construed as a log likelihood ratio between the original sample and the perturbed sample, assuming factorizable contributions of local and long-range dependencies to the overall likelihood. We expect to observe a larger $\log p_{LR}$ for ID data than OOD data.

Central to the success of this approach is identifying transformations that preserve local dependencies while disrupting long-range ones. We identify and explore two families of transformations that we call “stirring” and “shaking”.

3.5 Bijective transformations for robust outlier detection with PixelCNN++

3.5.1 Stirring.

We extend inversion solution by incorporating a family of 7 geometric transformations, including 3 rotations of the original image (by 90°, 180° or 270°), lateral inversion (mirror reflection about the vertical midline), and 3 rotations of the reflected image (again, by 90°, 180° or 270°). The $\log p_{LR}$ is summed across all 7 transformations to yield the final outlier detection score. We term the collection of these transformations as “stirring” (Fig. 4a). Because the individual transformations contribute additively, stirring produced a larger change in likelihoods for the perturbed images compared to the upright images (Fig. 4b, red density), than individual rotations (Fig. 4b, blue, orange, and green densities). Stirring may, thus, enable robust outlier detection for images with distinct axes of symmetry (Appendix C.4).

3.5.2 Shaking.

We consider a second class of bijective transformations that involve dividing the images into patches and shuffling these patches randomly (motivated in Appendix C.4). We consider three ways to achieve this: i) splitting the image in half along the horizontal midline, ii) splitting the image in half along the vertical midline and iii) splitting the images into four quarters along the horizontal and vertical midlines (Fig. 4d). These permit a total of 9 unique derangements – random permutations in which no patch is located in its original position.

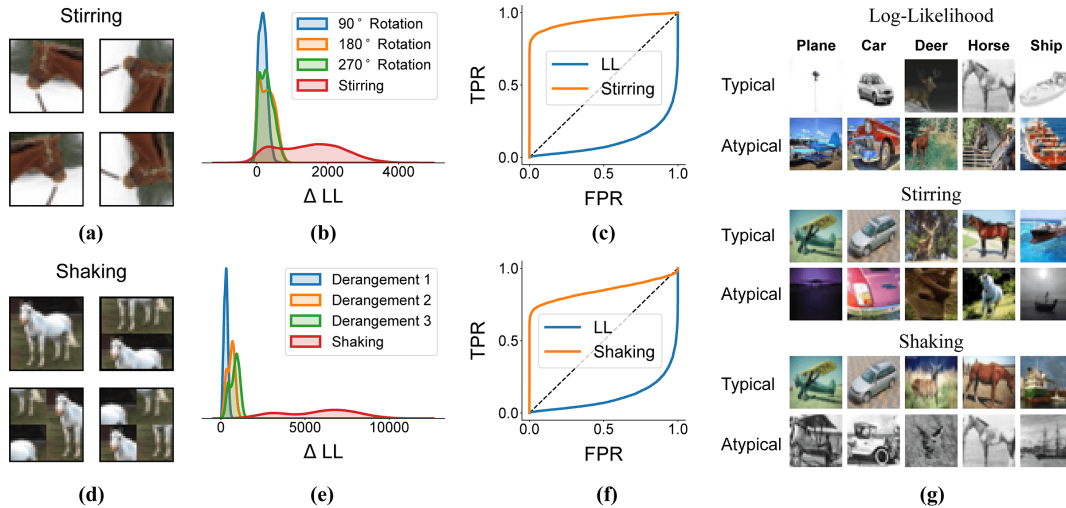


Figure 4. Robust outlier detection with stirring and shaking. (a) Examples of “stirring” transformations. (b) Change in PixelCNN++ LL after stirring, (red) as compared with rotations, applied individually (CIFAR10/ID). (c) ROC curve for outlier detection for CIFAR10/ID vs SVHN/OOD case using vanilla log-likelihood (blue) and stirring (orange). (d) Examples of “shaking” transformations (e, f) Same as in (b) and (c), but for shaking. (g) Specific sub-category of CIFAR10/ID images (columns) that were assigned among the highest and lowest vanilla log likelihoods $\log p(\mathbf{x})$ (top 2 rows), following stirring (middle 2 rows) or following shaking (bottom 2 rows).

$\log p_{LR}$ is summed across all 9 derangements to yield the final outlier detection score. We term the collection of these derangements as “shaking” (Fig 4d). Again, shaking produced a larger change in likelihoods for the perturbed images compared to the upright images, than individual derangements (Fig. 4e).

3.5.3 Conditional correction

. Our outlier detection score is a ratio of the logarithm of two probability densities: $p_{\theta}(\mathbf{x})$ and $p_{\theta}(\mathbf{x}')$. When $p_{\theta}(\mathbf{x})$ is a very small numerical value, the likelihood of the perturbed sample \mathbf{x}' , $p_{\theta}(\mathbf{x}')$ would also be comparably small numerically. In this case, it is likely, that the estimation of $\log p_{LR}$ would be noisy, and far from accurate (Appendix C.5). To avoid such noisy estimates, we adopt a pre-filtering strategy based on identifying outliers with the model log likelihood alone (Appendix C.5), following which shaking and stirring corrections are applied. We perform ablation experiments to estimate the contribution of this conditional correction.

4. Experiments

We train PixelCNN++ models on each of five grayscale image datasets: MNIST, FashionMNIST, EMNIST Letters, Sign Language MNIST¹, and CLEVR [16, 17, 18, 19]. Each of these models was tested against six OOD datasets which included the other four datasets as well as noise and constant images. Similarly, we trained PixelCNN++ models on each of six natural image datasets - SVHN, CelebA, CompCars, GTSRB, CIFAR10, and LSUN (classroom) [20, 21, 22, 23, 24, 25]. Each of the models was tested against seven OOD datasets

including noise and constant images. Details regarding the model architecture, datasets, training and testing are shown in Appendices A and B.

We report the area under the ROC curve (AUROC) between the respective test sets of the ID and OOD datasets in a 7×5 grid for grayscale and a 8×6 grid for natural image PixelCNN++ models (details in Appendix E). Area under the precision-recall (AUPRC) and false-positive rate at 80% true-positive rate (FPR@80%TPR) are reported in Appendix D. All results reported here include the conditional correction; results without the conditional correction are shown in Appendix F.

4.1 Outlier detection performance with stirring and shaking

First, we compared the outlier detection performance of $\log p_{LR}$ from “stirred” images against that of the vanilla log-likelihood for a PixelCNN++ trained on CIFAR10 images. We observed state-of-the-art AUROCs ($\sim 95\%$) with stirring for the particularly problematic case of CIFAR10 ID versus SVHN OOD (Fig. 4c). In addition, visually typical exemplars were assigned among the highest $\log p_{LR}$ (Fig. 4g, middle), whereas this was not the case using the vanilla log-likelihoods (Fig. 4g, top).

This superlative performance was observed across all other comparisons, comprising both grayscale and natural image datasets. In almost all cases, “stirring” (Fig. 5 and Fig. 6, orange symbols) outperformed vanilla LL (Fig. 5 and Fig. 6, blue symbols). Stirring achieved a performance near-ceiling in most of the grayscale cases. In the challenging cases of FMNIST/ID, CIFAR10/ID, and LSUN/ID, stirring achieved AUROCs of 95 and above. Overall, with stirring we saw an average AUROC improvement of $\sim 14\%$ for grayscale

¹<https://www.kaggle.com/datamunge/sign-language-mnist>

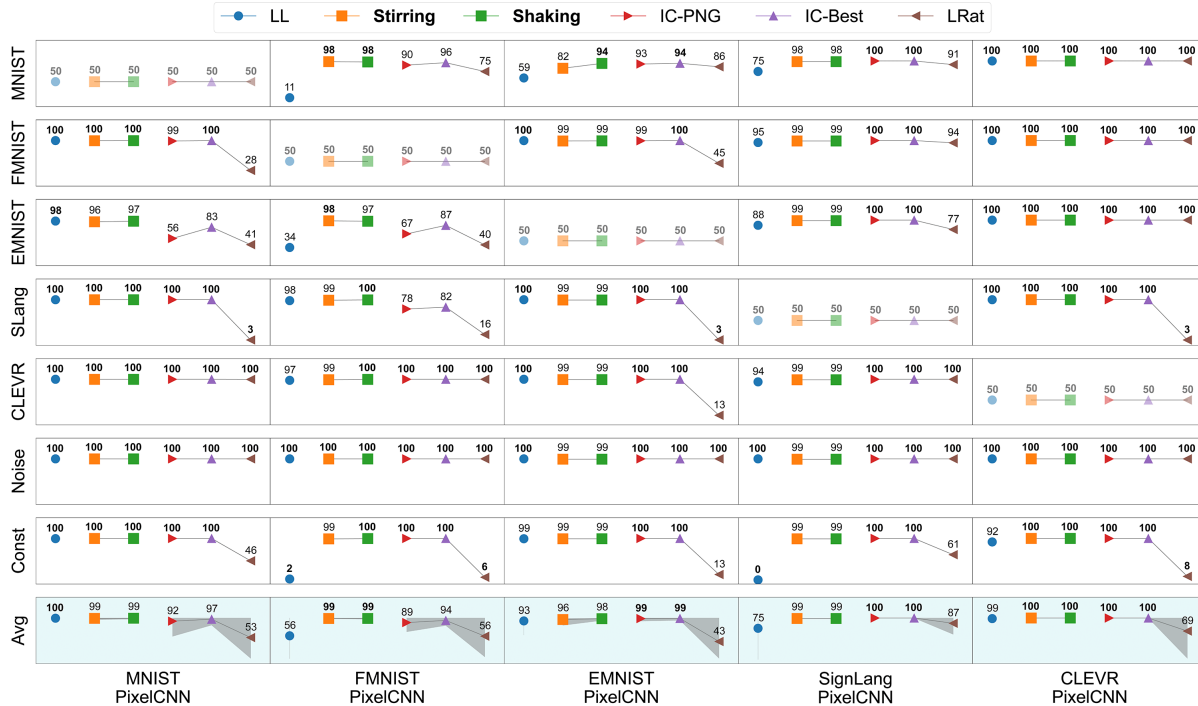


Figure 5. Outlier detection performance: Grayscale data. Outlier detection AUROC values for PixelCNNs trained with grayscale image datasets (ID, columns) and tested with other grayscale datasets (OOD, rows). Last row: average AUROC; gray shading: range of AUROC values. Blue: log likelihood (LL), uncorrected; Orange: Stirred LL; Green: Shaken LL; Red: Input Complexity (PNG); Purple: Input Complexity (Best); Brown: Likelihood Ratio. Numbers in bold: best performance.

images and $\sim 57\%$ for natural images.

We obtained similar results with $\log p_{LR}$ computed from “shaken” images also. Again, shaking improved outlier detection for the challenging case of CIFAR10/ID versus SVHN/OOD (Fig. 4f). In general, outlier detection with shaking improved across both grayscale and natural images (Fig. 5 and Fig. 6, green symbols), as compared to that with vanilla log-likelihoods. Overall, outlier detection performance improved, on average, by $\sim 14\%$ for grayscale images and $\sim 47\%$ for natural images, indicating marginally worse improvements than with shaking. Interestingly, with stirring, color information played a major role in determining atypical exemplars (Fig. 4g, lower). Additional results and ablation experiments are shown in Appendices F and G.

4.2 Comparison with competing methods

We compare our results with two state-of-the-art methods – Likelihood Ratios [2], and Input Complexity [8] – the two most relevant competing approaches for state-of-the-art outlier detection with PixelCNN++ (see section 2).

Our methods comfortably outperformed likelihood ratios (Fig. 5 and Fig. 6, filled red symbols) in all cases. Stirring performed $\sim 48\%$ better, on average, for grayscale images and $\sim 80\%$ better for natural images than likelihood ratios. Similarly, shaking performed $\sim 49\%$ better, on average, for grayscale images and $\sim 69\%$ better for natural images than likelihood ratios. The OOD detection numbers that we report for likelihood ratios are poorer than those reported by [2], who

used a more complex model architecture; these results suggest that the success of the likelihood ratio metric is architecture dependent.

Our metrics also outperformed or performed comparably with Input Complexity computed using the PNG compressor (Fig. 5 and Fig. 6; IC-PNG, brown symbols), or using the Best compressor (minimum compressed length; IC-Best, purple symbols). Stirring performed $\sim 6\%$ (2%) better, on average, for grayscale images and $\sim 14\%$ (5%) better for natural images than IC-PNG (IC-Best). Similarly, shaking performed $\sim 7\%$ (2%) better, on average, for grayscale images and $\sim 7\%$ (-2%) better for natural images than IC-PNG (IC-Best). Surprisingly, IC-Best did not perform well with specific datasets, like LSUN/ID or CIFAR10/ID on which our metrics, especially those based on stirring, performed exceedingly well.

5. Discussion

We developed simple, lightweight, and intuitive methods for state-of-the-art image outlier detection with PixelCNN++. Although our methods were tested on a particular type of deep autoregressive model our results may be relevant also for other classes of generative models (e.g. VAEs), whose likelihoods are readily biased by input image orientation [14]. Our methods may be relevant for outlier detection with other types of temporal data (e.g. speech), for which stirring and shaking can be readily performed, either by reversing the data in time, or by chunking and shuffling the sequence.

Across all 72 ID/OOD comparisons, “stirring” performed

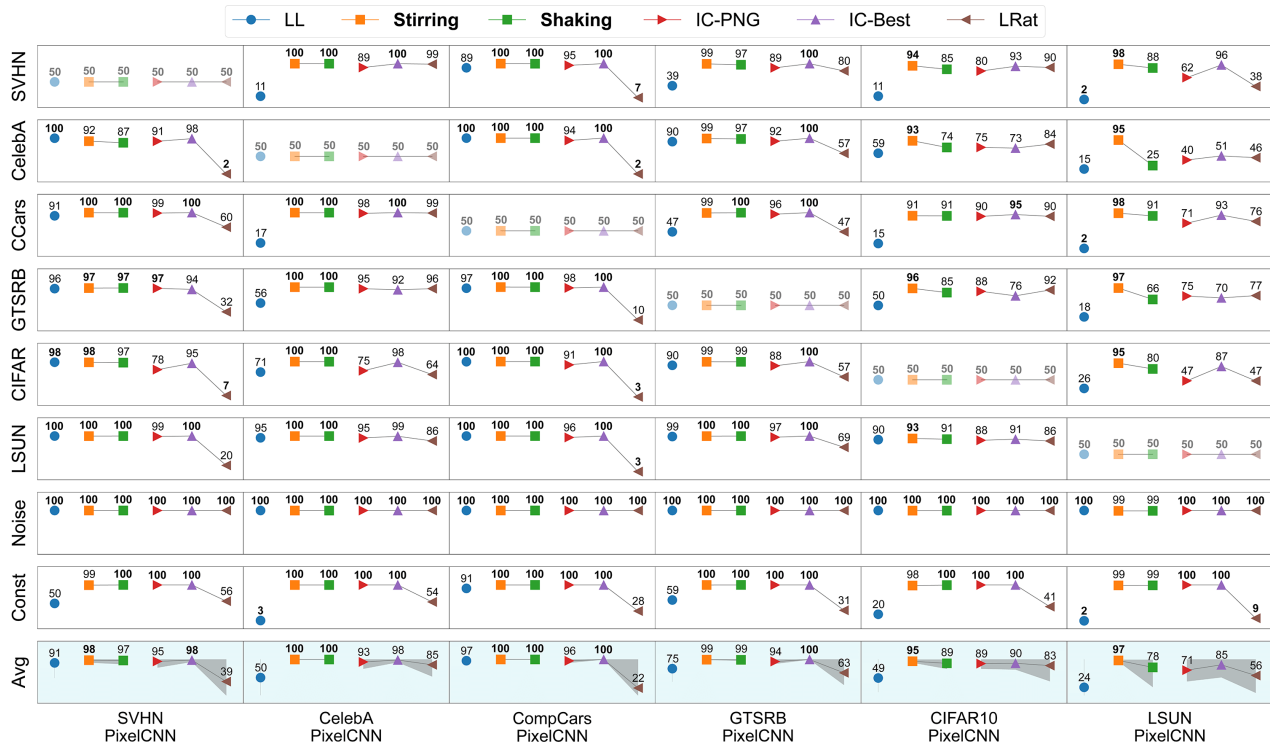


Figure 6. Outlier detection performance: Natural image data. Same as in Figure 5 but for natural image datasets.

noticeably worse than ceiling performance only with EMNIST/ID versus MNIST/OOD (AUROC of $\sim 82\%$), a not unreasonable failure given the feature similarity of MNIST and EMNIST samples (Appendix H). In fact, IC exhibited confusion for these two datasets also (MNIST/ID versus EMNIST/OOD, IC-Best AUROC $\sim 83\%$). On the other hand, while “shaking” performed well with most datasets, improvements were less impressive than those with stirring, especially for natural ID image datasets like CIFAR10 and LSUN (analyzed in Appendix I).

More generally, our results upend claims from a large body of recent literature: that deep generative models are unreliable for outlier detection [3, 2, 8]. We show that PixelCNN++ models are exquisitely sensitive to long-range dependencies in their training data, and isolating their contribution to PixelCNN++ likelihoods enables robust outlier detection.

References

- [1] Jasper Snoek, Hugo Larochelle, and Ryan P Adams. Practical bayesian optimization of machine learning algorithms. In *Advances in Neural Information Processing Systems*, volume 25, 2012.
- [2] Jie Ren, Peter J. Liu, Emily Fertig, Jasper Snoek, Ryan Poplin, Mark Depristo, Joshua Dillon, and Balaji Lakshminarayanan. Likelihood ratios for out-of-distribution detection. In *Advances in Neural Information Processing Systems*, volume 32, 2019.
- [3] Eric T. Nalisnick, Akihiro Matsukawa, Yee Whye Teh, Dilan Görür, and Balaji Lakshminarayanan. Do deep generative models know what they don’t know? In *7th International Conference on Learning Representations, ICLR 2019*, 2019.
- [4] Hyunsun Choi, Eric Jang, and Alexander A. Alemi. WAIC, but Why? Generative Ensembles for Robust Anomaly Detection. *arXiv e-prints*, page arXiv:1810.01392, October 2018.
- [5] Zhisheng Xiao, Qing Yan, and Yali Amit. Likelihood regret: An out-of-distribution detection score for variational auto-encoder. In *Advances in Neural Information Processing Systems*, volume 33, pages 20685–20696, 2020.
- [6] Aäron Van Den Oord, Nal Kalchbrenner, and Koray Kavukcuoglu. Pixel recurrent neural networks. In *Proceedings of the 33rd International Conference on International Conference on Machine Learning - Volume 48*, ICML’16, page 1747–1756, 2016.
- [7] Tim Salimans, Andrej Karpathy, Xi Chen, and Diederik P. Kingma. Pixelcnn++: Improving the pixelcnn with discretized logistic mixture likelihood and other modifications. In *5th International Conference on Learning Representations, ICLR 2017, Conference Track Proceedings*, 2017.
- [8] Joan Serrà, David Álvarez, Vicenç Gómez, Olga Sliozovskaia, José F. Núñez, and Jordi Luque. Input complexity and out-of-distribution detection with likelihood-based generative models. In *8th International Conference on Learning Representations, ICLR 2020, Conference Track Proceedings*, 2020.

- [9] Balaji Lakshminarayanan, Alexander Pritzel, and Charles Blundell. Simple and scalable predictive uncertainty estimation using deep ensembles. In *Advances in Neural Information Processing Systems*, volume 30, 2017.
- [10] Shiyu Liang, Yixuan Li, and R. Srikant. Enhancing the reliability of out-of-distribution image detection in neural networks. In *6th International Conference on Learning Representations, ICLR 2018, Conference Track Proceedings*, 2018.
- [11] Jerone Andrews, Edward Morton, and Lewis Griffin. Detecting anomalous data using auto-encoders. *International Journal of Machine Learning and Computing*, 6:21, 01 2016.
- [12] Lukas Ruff, Robert Vandermeulen, Nico Goernitz, Lucas Deecke, Shoaib Ahmed Siddiqui, Alexander Binder, Emmanuel Müller, and Marius Kloft. Deep one-class classification. In Jennifer Dy and Andreas Krause, editors, *Proceedings of the 35th International Conference on Machine Learning*, volume 80 of *Proceedings of Machine Learning Research*, pages 4393–4402, 10–15 Jul 2018.
- [13] Eric T. Nalisnick, Akihiro Matsukawa, Yee Whye Teh, and Balaji Lakshminarayanan. Detecting out-of-distribution inputs to deep generative models using a test for typicality. *arXiv preprint arXiv:1906.02994*, 2019.
- [14] Kushal Chauhan, Barath Mohan U, Pradeep Shenoy, Manish Gupta, and Devarajan Sridharan. Robust outlier detection by de-biasing vae likelihoods. In *Proceedings of the IEEE/CVF Conference on Computer Vision and Pattern Recognition (CVPR)*, pages 9881–9890, June 2022.
- [15] Polina Kirichenko, Pavel Izmailov, and Andrew G Wilson. Why normalizing flows fail to detect out-of-distribution data. In *Advances in neural information processing systems*, volume 33, pages 20578–20589, 2020.
- [16] Li Deng. The mnist database of handwritten digit images for machine learning research. *IEEE Signal Processing Magazine*, 29(6):141–142, 2012.
- [17] Han Xiao, Kashif Rasul, and Roland Vollgraf. Fashion-mnist: a novel image dataset for benchmarking machine learning algorithms. *arXiv preprint arXiv:1708.07747*, 2017.
- [18] Gregory Cohen, Saeed Afshar, Jonathan Tapson, and André van Schaik. Emnist: an extension of mnist to handwritten letters. *arXiv preprint arXiv:1702.05373*, 2017.
- [19] Justin Johnson, Bharath Hariharan, Laurens Van Der Maaten, Li Fei-Fei, C Lawrence Zitnick, and Ross Girshick. Clevr: A diagnostic dataset for compositional language and elementary visual reasoning. In *Proceedings of the IEEE/CVF Conference on Computer Vision and Pattern Recognition (CVPR)*, pages 2901–2910, 2017.
- [20] Yuval Netzer, Tao Wang, Adam Coates, Alessandro Bisaccho, Bo Wu, and Andrew Y. Ng. Reading digits in natural images with unsupervised feature learning. In *NIPS Workshop on Deep Learning and Unsupervised Feature Learning 2011*, 2011.
- [21] Ziwei Liu, Ping Luo, Xiaogang Wang, and Xiaoou Tang. Deep learning face attributes in the wild. In *2015 IEEE International Conference on Computer Vision, ICCV 2015*, pages 3730–3738, 2015.
- [22] Linjie Yang, Ping Luo, Chen Change Loy, and Xiaoou Tang. A large-scale car dataset for fine-grained categorization and verification. In *2015 IEEE Conference on Computer Vision and Pattern Recognition (CVPR)*, pages 3973–3981, 2015.
- [23] Johannes Stallkamp, Marc Schlipsing, Jan Salmen, and Christian Igel. The German Traffic Sign Recognition Benchmark: A multi-class classification competition. In *IEEE International Joint Conference on Neural Networks*, pages 1453–1460, 2011.
- [24] Alex Krizhevsky. Learning multiple layers of features from tiny images. Technical report, 2009.
- [25] Fisher Yu, Yinda Zhang, Shuran Song, Ari Seff, and Jianxiong Xiao. Lsun: Construction of a large-scale image dataset using deep learning with humans in the loop. *arXiv preprint arXiv:1506.03365*, 2015.
- [26] Diederik P. Kingma and Jimmy Ba. Adam: A method for stochastic optimization. In *3rd International Conference on Learning Representations, ICLR 2015, Conference Track Proceedings*, 2015.
- [27] Christophe Leys, Christophe Ley, Olivier Klein, Philippe Bernard, and Laurent Licata. Detecting outliers: Do not use standard deviation around the mean, use absolute deviation around the median. *Journal of Experimental Social Psychology*, 49(4):764–766, 2013.

Appendices

A. Model Architecture and Training

Table 1. PixelCNN++ architecture Parameters used in TensorFlow Probability’s implementation of PixelCNN++.

Parameter	Grayscale	Natural
image_shape	(32, 32, 1)	(32, 32, 3)
conditional_shape *	None	None
num_resnet	2	2
num_hierarchies	4	4
num_filters	32	64
num_logistic_mix	5	5
receptive_field_dims *	(3, 3)	(3, 3)
dropout_p	0.3	0.3
resnet_activation *	‘concat_elu’	‘concat_elu’
use_weight_norm *	True	True
use_data_init *	True	True
high *	255	255
low *	0	0
dtype *	tf.float32	tf.float32

* indicates arguments where we used TensorFlow defaults

We use TensorFlow Probability’s² implementation of PixelCNN++. Unlike the older PixelCNN model, PixelCNN++ employs downsampling and upsampling at specific layers to capture long range correlations. We follow the same idea and employ an architecture similar to that in the original PixelCNN++ paper. Our model consists of 8 blocks of 2 residual layers each. We use 64 (3×3) convolutional filters in all layers for natural images and 32 (3×3) convolutional filters for grayscale images. Between the first and the second blocks, second and the third blocks, and third and the fourth blocks we perform downsampling by a factor of 2 with strided convolutions. We place a skip (identity) connection between the fourth and the fifth blocks. We perform upsampling by a factor of 2 using strided transpose convolutions between the fifth and the sixth blocks, sixth and seventh blocks, and seventh and eighth blocks. One key difference with the standard PixelCNN++ model is that our hierarchies are 4 levels deep, so that our model has 32×32, 16×16, 8×8 and 4×4 size convolutional layers (Fig. 1a). The inner layers were introduced in PixelCNN++ specifically to capture long-range dependencies [7] – a feature absent in the original PixelCNN model [6] – and our architecture increases the nesting of the inner layers by having one level more.

In addition, we employ short-cut connections between residual layers of matched size. In particular blocks one and eight, two and seven, three and six, four and five are connected using short-cut dense connections (Fig. 1a, curved, dashed). We perform regularization by setting the dropout parameter to 0.3. Finally, we employ a mixture of 5 logistics

²<https://www.tensorflow.org/probability>

to approximate the categorical likelihoods. The parameters of “tf.distributions.PixelCNN” to replicate our model architecture are shown in Table. 1.

We train each model for 100 epochs with a batch size of 32 and a learning rate of 0.001 using the Adam optimizer [26]. The parameters at the epoch corresponding to the least validation loss (negative log likelihood) were selected using training checkpoints and used for evaluation.

B. Datasets and Preprocessing

Nearly all of our datasets are available in the TensorFlow Datasets³ library, except for CelebA [21], GTSRB [23], CompCars [22], and Sign Language MNIST⁴; the latter were manually downloaded from their respective sources. For EMNIST dataset we only use the “letters” subset, while for LSUN we use the “classroom” (default) subset. All images were loaded as 8-bit images and resized to 32 × 32 pixels (x × y).

We set apart 10% of the training samples for validation while the evaluation was performed on the designated test splits of each dataset. As the LSUN classroom dataset has only 300 samples in its test set, we set apart another 10% from the training set (in addition to the validation set) for evaluation. The list of datasets used along with the number of samples in the train, validation, and test splits are shown in Table. 2, along with example images from each dataset.

C. De-biasing PixelCNN++ likelihoods: Additional results

C.1 Bias in PixelCNN++ likelihoods for grayscale images













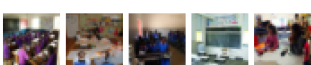


In section 3, we analyzed the origins of bias in PixelCNN++ likelihoods for natural image datasets (CIFAR10/ID vs SVHN/OOD). We observed that the reconstruction error and scale were lower for the OOD samples and the log likelihood was higher for OOD samples than for ID samples, leading to anomalous outlier detection AUROCs (Fig. 1h). Here, we analyze another, well-reported challenging case for outlier detection with grayscale images – FashionMNIST (or FMNIST)/ID vs MNIST/OOD.

In this case, we found that reconstruction errors were marginally lower for FMNIST/ID images (Fig. 7a, blue density) as compared to the MNIST/OOD images (Fig. 7a, orange density). Yet, the scale was markedly lower for MNIST/OOD images (Fig. 7b, orange density) than for the FMNIST/ID images (Fig. 7b, blue density). Despite higher reconstruction errors, the lower scale sufficed to yield higher likelihoods for MNIST/OOD samples (Fig. 7c, orange density) as compared to FMNIST/ID samples (Fig. 7c, blue density); this resulted in anomalous outlier detection AUROC curves (Fig. 7d, bowed downwards).

³<https://www.tensorflow.org/datasets>

⁴<https://www.kaggle.com/datamunge/sign-language-mnist>

Table 2. Dataset details. List of datasets used for evaluating outlier detection with PixelCNN++.

Dataset	Type	Exemplars	N-train (N-val)	N-test
MNIST	Grayscale		54000 (6000)	10000
Fashion-MNIST	Grayscale		54000 (6000)	10000
EMNIST-Letters	Grayscale		79920 (8880)	14800
Sign Language MNIST	Grayscale		24720 (2735)	7172
CLEVR	Grayscale		63000 (7000)	15000
Gray-Noise	Grayscale		-	10000
Gray-Constant	Grayscale		-	256
SVHN	Color		65932 (7325)	26032
CelebA	Color		146493 (16277)	19962
CompCars	Color		28034 (3114)	13333
GTSRB	Color		35289 (3920)	12630
CIFAR-10	Color		45000 (5000)	10000
LSUN-Classroom	Color		134504 (16813)	16813
Color-Noise	Color		-	10000
Color-Constant	Color		-	10000

In other words, more confident PixelCNN++ predictions for MNIST/OOD as compared to FMNIST/ID resulted in anomalous likelihoods for OOD samples poor outlier detection. The greater confidence is likely a result of the large number of black background pixels in the MNIST dataset [2]: these background pixels can be readily predicted by the PixelCNN++ model simply by examining a local neighborhood of preceding pixel values.

C.2 Comparing PixelCNN++ likelihoods and input complexity (IC): Methods

In section 3.2 (main text), we used constant, noise, and repeating color sequence images to show the mapping between PixelCNN++ likelihoods and compressed lengths. These images were all 3 channel images and were generated as follows:

Constant: These represent uniformly colored images. Three random integers were independently sampled from a uniform distribution in the range $[0,255]$ – one for each of the red, green, and blue channels. Each channel assumes the same value across all pixels in the image, thereby producing a uniform colored 8-bit image.

Noise: These represent noise images with independent sub-pixel. Each sub-pixel was randomly and independently sampled from a uniform distribution in the range $[0,255]$.

Color Sequence: These represent images with periodic sequences of colors. For example, a Color-Seq 50 image contained 50 randomly sampled colors arranged as a repeating sequence, and a Color-Seq 2 is an alternating checkerboard pattern. More generally, for color-seq K , K random independent integers were sampled from a uniform distribution in

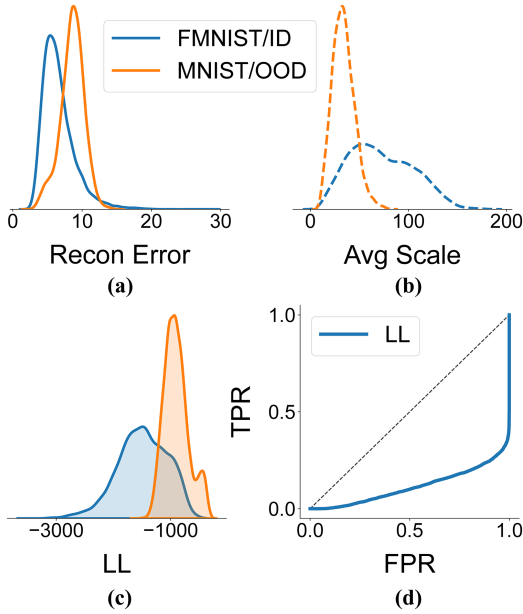


Figure 7. Biases in PixelCNN++ likelihoods for grayscale images. (a-d) Same as in Figures. 1e-h, respectively but for FMNIST/ID (blue) vs MNIST/OOD (orange).

the range [0,255] for each channel (3K integers in all). For each channel, its respective K intensities were placed in a raster scan order (row first), followed by repeating the same sequence of values until the end of the image was reached. This produced a repeating sequence of K colors in the image.

Using these images, we showed that the mapping between PixelCNN++ likelihoods and PNG compressed lengths was not even approximately linear. Here, we show that our claims are consistent with other compressors like JPEG (Fig. 8a) and FLIF (Fig. 8b). We also observed similar results when considering the “best” compressor (Fig. 8c) which is computed as the minimum size for a given image across the three compressors $L(\mathbf{x}) = \min(L_1(\mathbf{x}), L_2(\mathbf{x}), L_3(\mathbf{x}))$.

In summary, regardless of the compressor used, widely different log-likelihoods occurred for images with identical compressed lengths (Fig. 8, dashed horizontal lines) and, conversely, images with closely similar log-likelihoods exhibited widely different compressed lengths (Fig. 8, dashed vertical lines).

C.3 PixelCNN++ ablation experiments: Methods

We performed two kinds of ablation experiments: a) by removing the symmetric convolutional blocks (or hierarchies) of the PixelCNN++ network (Fig. 3a, boxes), and b) by removing the short-cut connections (Fig. 3a, curved, dashed arrows). We quantified the effect of each type of ablation on model likelihoods.

For the first series of experiments (a), we sought to measure the contribution of the 4x4, 8x8 and 16x16 blocks to the pixel level predictions in terms of both the location and scale parameters. Although we could not remove the 8x8 or 16x16 layers individually, due to the nested (sequential)

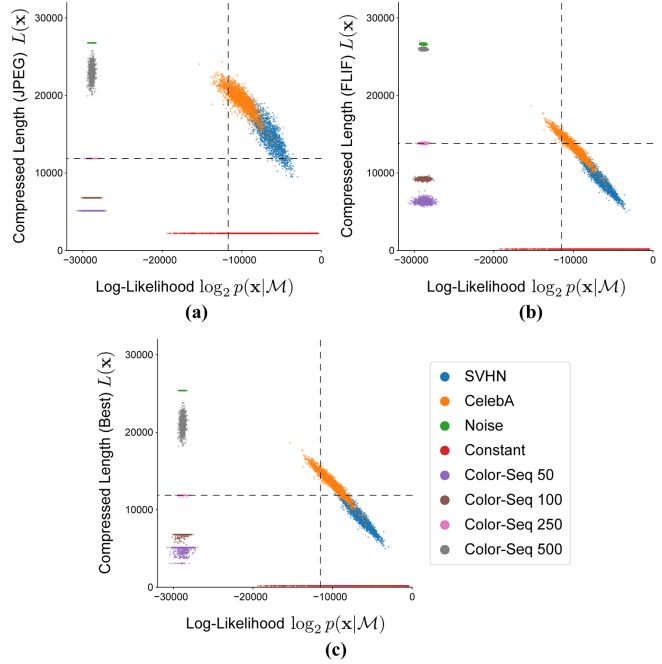


Figure 8. Compressed lengths have a many-to-one relationship with PixelCNN++ likelihoods across compression techniques. Same as in Figure 2 but by using (a) JPEG, (b) FLIF, and (c) Best compressors for computing the compressed lengths.

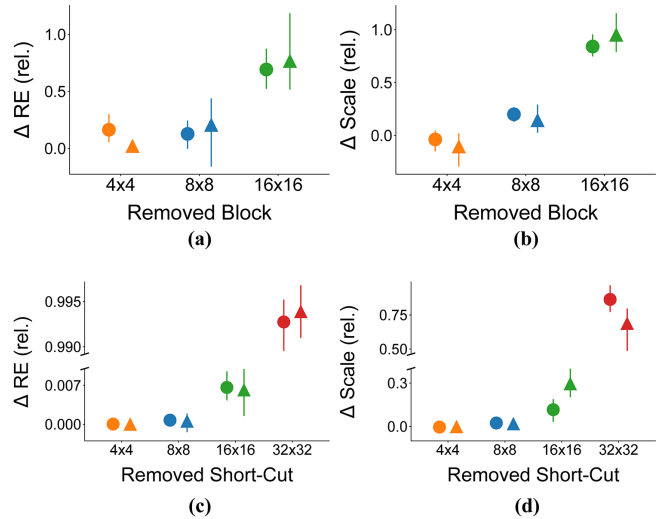


Figure 9. PixelCNN++ relies heavily on local dependencies for prediction. (a, b) Same as in Figure 3b but showing the effect of block ablations on reconstruction error and scale respectively. (c, d) Same as in Figure 3c but showing the effect of short-cut ablations on reconstruction error and scale respectively.

layout of these layers, we quantified their contribution to the model log likelihood (LL) as follows: the contribution of the $K \times K$ layers was quantified as the change in LL upon removing all innermost layers up to size $K \times K$ minus the change in LL upon removing all innermost layers up to size $K/2 \times K/2$. For example the contribution of the 8x8 layers was quantified

as the change in LL upon removing the two (4×4 and 8×8) innermost layers minus the change in LL upon removing the 4×4 layer alone. The outermost (32×32) block could not be removed because that would entail ablating virtually the entire PixelCNN++ network (Fig. 3a). Each of these changes in LL were normalized (divided) by the changes in LL upon removing all 3 sets of blocks, to quantify the relative magnitude of the contribution of each block; the normalization was done separately for the ID and OOD data.

For the second series of experiments (b), we ablated short-cut connections across each symmetric pair of blocks (4×4 , 8×8 , 16×16 , and 32×32) independently of the other connections (Fig. 3a, curved, dashed arrows). In this case also, changes in LL were normalized (divided) by the changes in LL upon removing all 4 sets of short-cut connections, to quantify the relative magnitude of the contribution of each set of connections. Note that in Figure 3c there is a break in the y-axis indicating the inordinately high effect on LL upon removing the 32×32 block’s short-cut connections.

In Figures 3b-c, we showed the effects of ablation on log likelihoods. Here, we also show that these changes in likelihoods are accompanied by progressively higher reconstruction errors (Fig. 9a, c) and more uncertain predictions (Fig. 9b, d). As with the likelihoods, the largest effects on reconstruction error and scale occur for the outermost layers (16×16 for block ablation and 32×32 for short-cut connection ablation), which capture the most local dependencies in the model.

C.4 Stirring and Shaking: Motivation

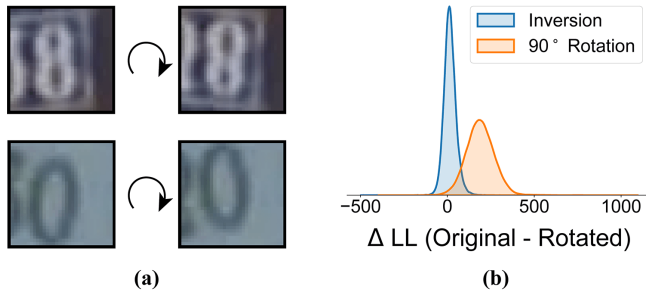


Figure 10. Motivation for Stirring. (a) Exemplars from the SVHN dataset before and after inversion illustrating a horizontal axis of near-symmetry in these images. (b) Difference between the log likelihoods of the original and transformed SVHN/ID images with inversion (blue) and with 90° rotation (orange).

Motivation for stirring. In the main text, we had shown how likelihoods for inverted faces were substantially lower than those for upright faces for a PixelCNN++ model trained on the CelebA dataset (Fig. 3d-e). We had shown also how this was likely a result of the model having learned long-range dependencies in the ID, but not OOD, data.

While inversion works well to isolate long-range dependencies for images that have a natural, upright orientation (e.g. faces or cars), such a perturbation may not work well for all datasets. For example, in datasets like SVHN, images of

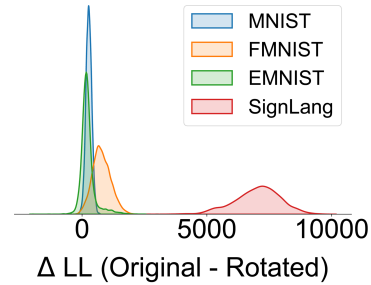


Figure 11. Motivation for Shaking. $\log p_{LR}$ based on stirring for MNIST/ID (blue), EMNIST/ID (green), FashionMNIST/ID (orange) and SignLang/ID (red), with PixelCNN++ models trained on the respective datasets.

certain digits may have a clear, horizontal axis of symmetry (e.g. 0-s, 1-s or 8-s) (Fig. 10a). Or certain digits may resemble others when inverted (e.g. 6-s and 9-s). In these cases, if the inverted inlier image is substantially visually similar to an upright inlier image, then the PixelCNN++ model would yield similar likelihoods for both inverted and upright images. Indeed this is what we observed when we compared PixelCNN++ likelihoods for inverted and upright images with a model trained on the SVHN dataset (Fig. 10b, blue density); note that mode of the $\Delta LL (=LL\text{-upright} - L\text{-inverted})$ density is around zero. To ameliorate this challenge, one may then consider a different rotational transformation that is not vulnerable to this symmetry. For example, a 90° clockwise rotation yielded significantly lower likelihoods for the rotated inlier images than for upright images in the SVHN dataset (Fig. 10b, orange density); note that mode of the ΔLL density is clearly greater than zero. Consequently, we considered a full family of transformations including rotation by different angles of the upright and the flipped images. This collection of transformation is what we call “stirring”.

Motivation for shaking. Despite stirring, some types of images may comprise features of such simplicity that a powerful PixelCNN++ model trained on upright images alone could reconstruct stirred images accurately and confidently. We note that this happens primarily in simplistic grayscale datasets like MNIST and EMNIST, but not for more complex grayscale image datasets like FashionMNIST and SignLanguageMNIST (Fig. 11). For these datasets, likelihoods for the original and stirred images largely overlap, likely because edges, contours and other simple features associated with digits and letters are simple enough for the PixelCNN++ model to predict, regardless of the orientation of the images. In these cases, estimating the contribution of long-range dependencies to the log likelihood ($\log p_{LR}$) becomes challenging with stirring. Consequently, we consider a second class of bijective transformations that involve dividing the images into patches and randomly shuffling these patches spatially.

Specifically, we consider the following schemes for patching and shuffling the images: i) 1 derangement by splitting the image in half along the horizontal mid-line, ii) 1 derangement by splitting the image in half along the vertical mid-line; iii) 9

derangements by splitting the image into four quarters and shuffling. 2 derangements in scheme (iii) are redundant with the derangements in (i) and (ii). Thus, we obtain a total of 9 unique derangements across the 3 schemes. This collection of derangements is what we call “shaking”.

C.5 Conditional Correction: Methods

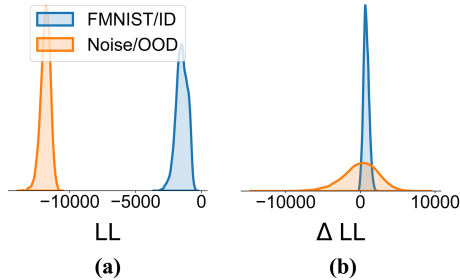


Figure 12. Motivation for conditional correction. (a) Log likelihood of Noise/OOD samples (orange) and FMNIST/ID samples (blue) for a PixelCNN++ trained on the FMNIST dataset. (b) $\log p_{LR}$ based on stirring for Noise/OOD samples (orange) and for FMNIST/ID samples (blue).

The $\log p_{LR}$ based on either shaking or stirring can be a noisy estimate, especially when the likelihoods involved are very small numbers. We illustrate this with an example of a PixelCNN++ model trained on the FMNIST dataset; we observe that the log-likelihood for Noise/OOD is many orders of magnitude smaller than that for FMNIST/ID (Fig. 12a). As a result, the $\log p_{LR}$ based on stirring has a much larger variance across samples for the Noise/OOD than for the FMNIST/ID dataset (Fig. 12b).

To ameliorate this challenge, we adopt the following rational strategy for outlier detection. We first identify outliers below the left-tail of the log-likelihood distribution of the training data as being below 3 times the median absolute deviation (3-MAD) of the median [27]. When a test sample’s log-likelihood falls below the 3-MAD criterion, it is directly labeled as an outlier. After filtering based on this condition, only samples whose log-likelihood overlaps with the training log-likelihood distribution are considered for our corrections with the shaking and stirring transformations.

All of the outlier detection results with shaking and stirring reported in the main text (Figs. 5 and 6) include the conditional correction; results without the conditional correction are shown in Appendix F.

D. Outlier Detection: Additional Results

The results in the main text quantify outlier detection performance using Area Under the Receiver Operating Characteristic (AUROC) curve (Figs. 5 and 6). The ROC is a plot of true-positive rate versus false-positive rates, and a higher AUROC indicates better outlier detection. All AUROC results are shown for distinguishing ID test versus OOD test samples. For uniformity across all comparisons, we sampled 5000 images randomly from the test split of each of the datasets and

computed the AUROC; random seeds and code are available for reproducing these results (see Appendix J).

Here, we show outlier detection performance using the area under the precision-recall curve (AUPRC) (Fig. 13a for grayscale images and Fig. 13b for natural images) and false-positive rate at 80% true-positive rate (FPR@80%TPR) (Fig. 14a for grayscale images and Fig. 14b for natural images). Higher values of AUPRC, and lower values of FPR@80%TPR, indicate better outlier detection. All metrics were calculated using the scikit-learn⁵ library.

Similar to the results based on AUROC, these metrics (AUPRC and FPR@80%TPR) also show that stirring or shaking show substantial improvements over vanilla log-likelihoods for outlier detection.

E. Comparison with Competing Approaches

For evaluating competing approaches (Input Complexity and Likelihood Ratios) we use the same PixelCNN++ architecture as mentioned in Appendix A.

Likelihood Ratio: The likelihood ratio [2] was computed using our standard PixelCNN++ models as the foreground models. The background models were trained by corrupting the input data with uniform random noise with a mutation rate $\mu=0.1$ for grayscale datasets and $\mu = 0.3$ for natural image datasets, following the recommendation of the original study. The OOD detection score was then computed as the difference between the log likelihood assigned by the foreground model and that assigned by the background model for the original test sample (Figs. 5 and 6, brown symbols).

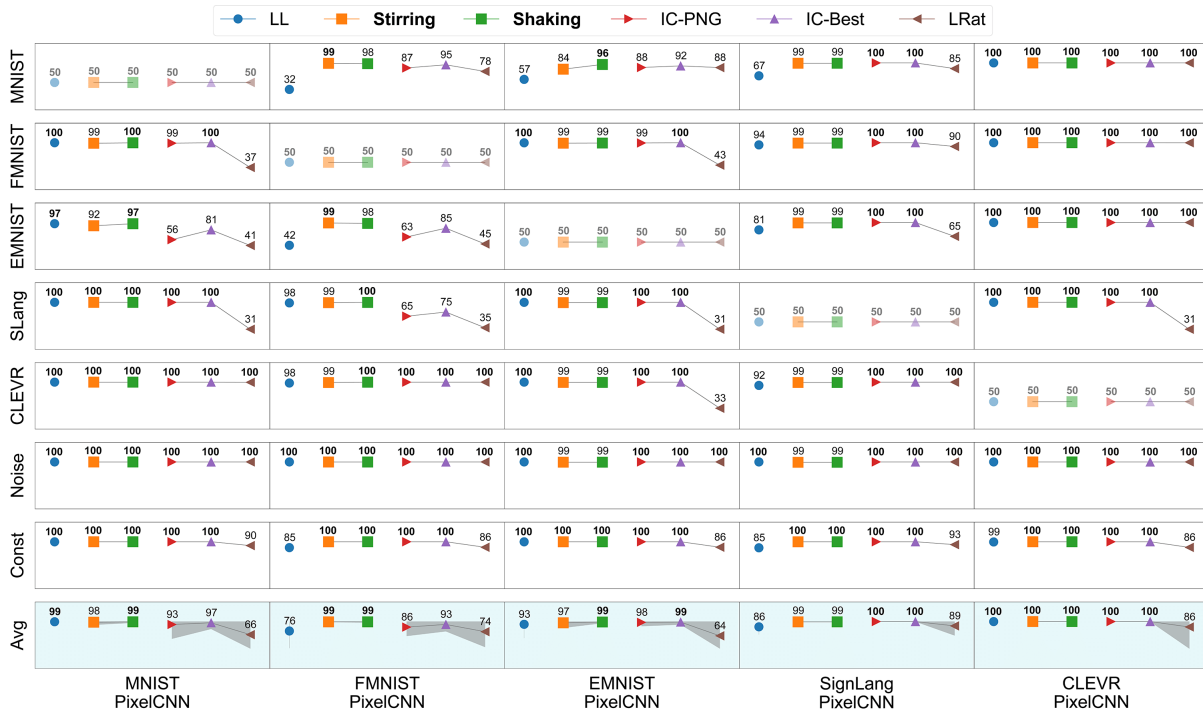
Our implementation of likelihood ratio yielded slightly worse AUROC values than those reported by [2] (Table 3, first and second rows), possibly because their study employed a more complex PixelCNN++ architecture. AUROC values with stirring (our method) are, nevertheless, comparable to state-of-the-art values reported by [2] (Table 3, last row).

Table 3. AUROC for outlier detection based on Likelihood Ratios (LRat) (First row) LRat AUROC for outlier detection as reported in [2]. (Second row) LRat AUROC based on our PixelCNN++ implementation. (Third row) Stirring AUROC. (First column) FMNIST/ID vs MNIST/OOD (Second column) CIFAR10/ID vs SVHN/OOD.

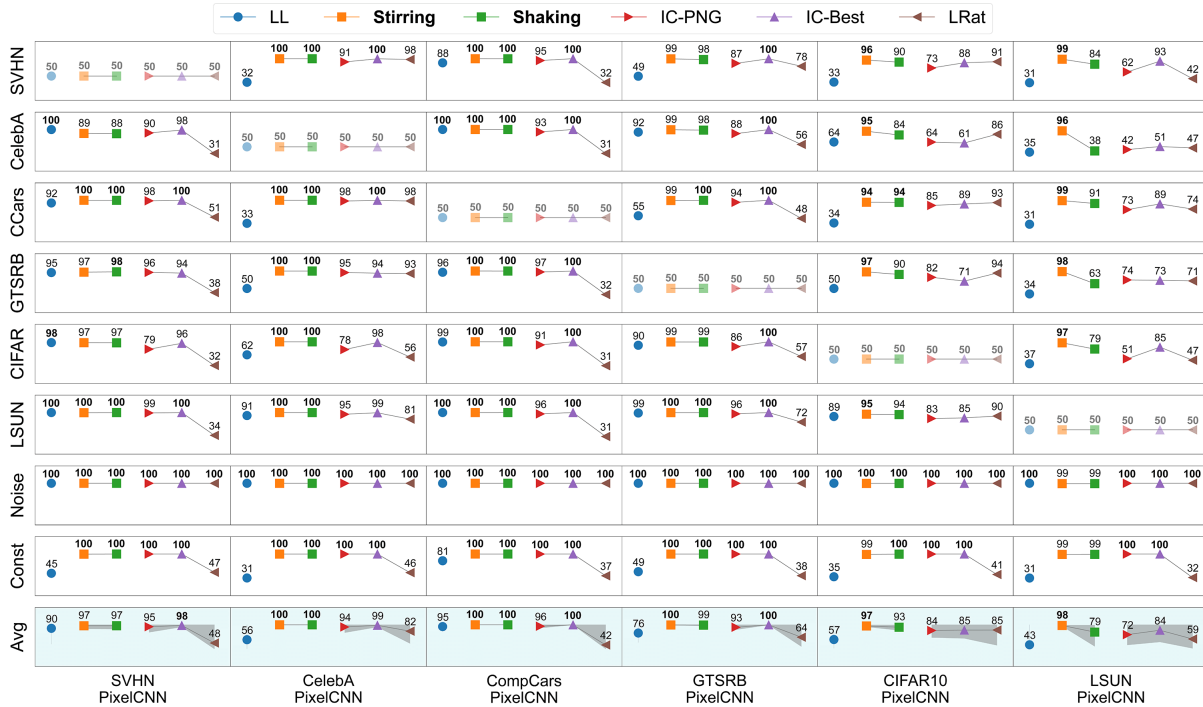
Method	FM vs MN	CF vs SV
LRat (orig paper)	99	93
LRat (our implem)	75	90
Stirring (our method)	98	94

Input Complexity: The input complexity (IC) metric [8] was computed as $S(\mathbf{x}) = -\ell_{\mathcal{M}}(\mathbf{x}) - L(\mathbf{x})$, where $\ell_{\mathcal{M}}(\mathbf{x})$ is the log likelihood (in log base 2) and $L(\mathbf{x})$ is the complexity estimates in bits for the image \mathbf{x} . We report results using PNG

⁵<https://scikit-learn.org/stable/>



(a)

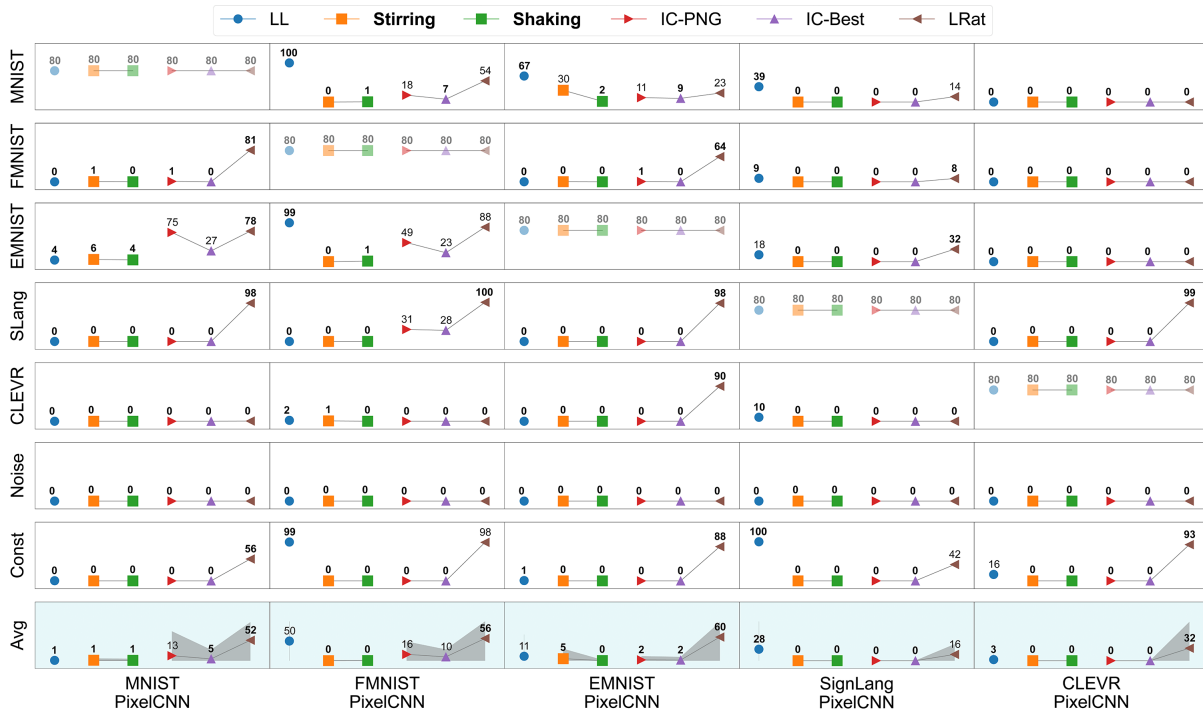


(b)

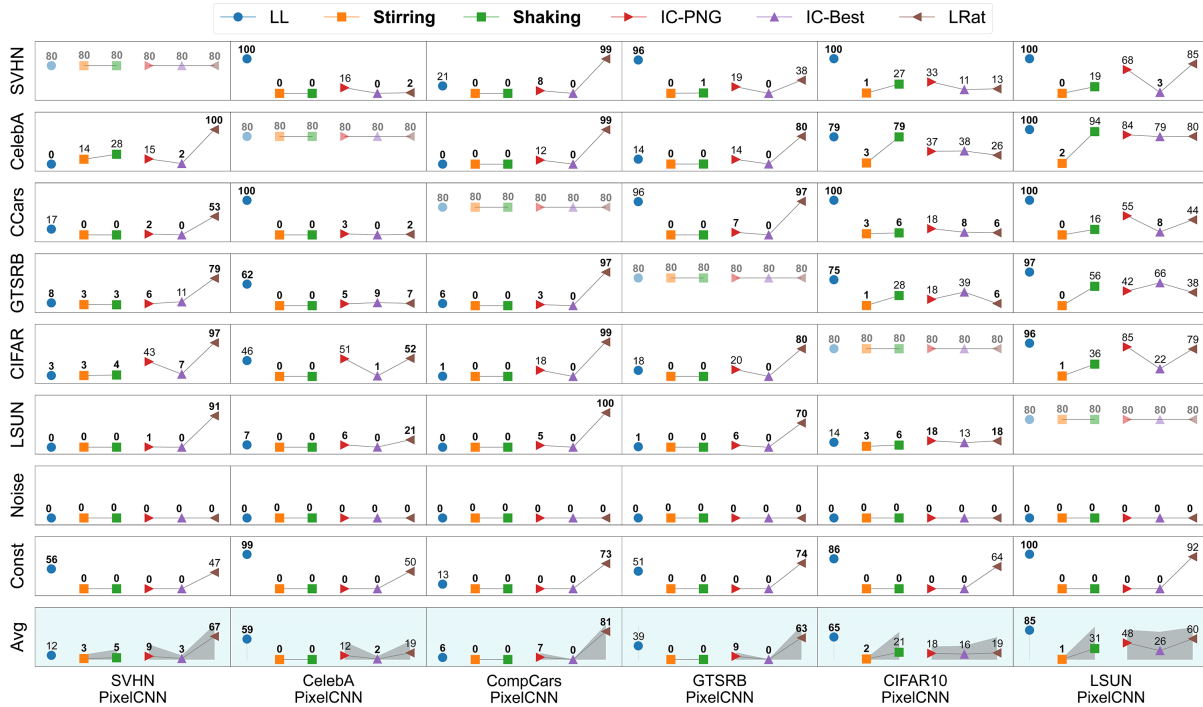
Figure 13. Outlier detection performance measured using area under the precision-recall curve. (a) Same as in Figure 5 but results are shown using area under the precision-recall curve (AUPRC) instead of AUROC. **(b)** Same as in Figure 6 but results are shown using AUPRC instead of AUROC. Higher values indicate better outlier detection performance. Other conventions are the same as in Figures 5-6.

compression for the complexity estimate; these are reported as IC-PNG (Figs. 5 and 6, red symbols). We also estimated the score using the best complexity estimate as $\min(L_1, L_2, L_3)$

using the JPEG, PNG, and FLIF compression algorithms; these are reported as IC-Best (Figs. 5 and 6, purple symbols).



(a)



(b)

Figure 14. Outlier detection performance measured using false-positive rate at 80% true-positive rate. (a) Same as in Figure 5 but results are shown using false-positive rate at 80% true-positive rate (FPR@80%TPR) instead of AUROC. **(b)** Same as in Figure 6 but results are shown using FPR@80%TPR instead of AUROC. Lower values indicate better outlier detection performance. Other conventions are the same as in Figures 5-6.

F. Results without conditional correction

All the results with stirring and shaking in Figures 5 and 6 include the conditional correction as detailed in Appendix

C.5. Here, we show AUROC for outlier detection without conditional correction for grayscale images in Figure 15a and for natural images in Figure 15b.

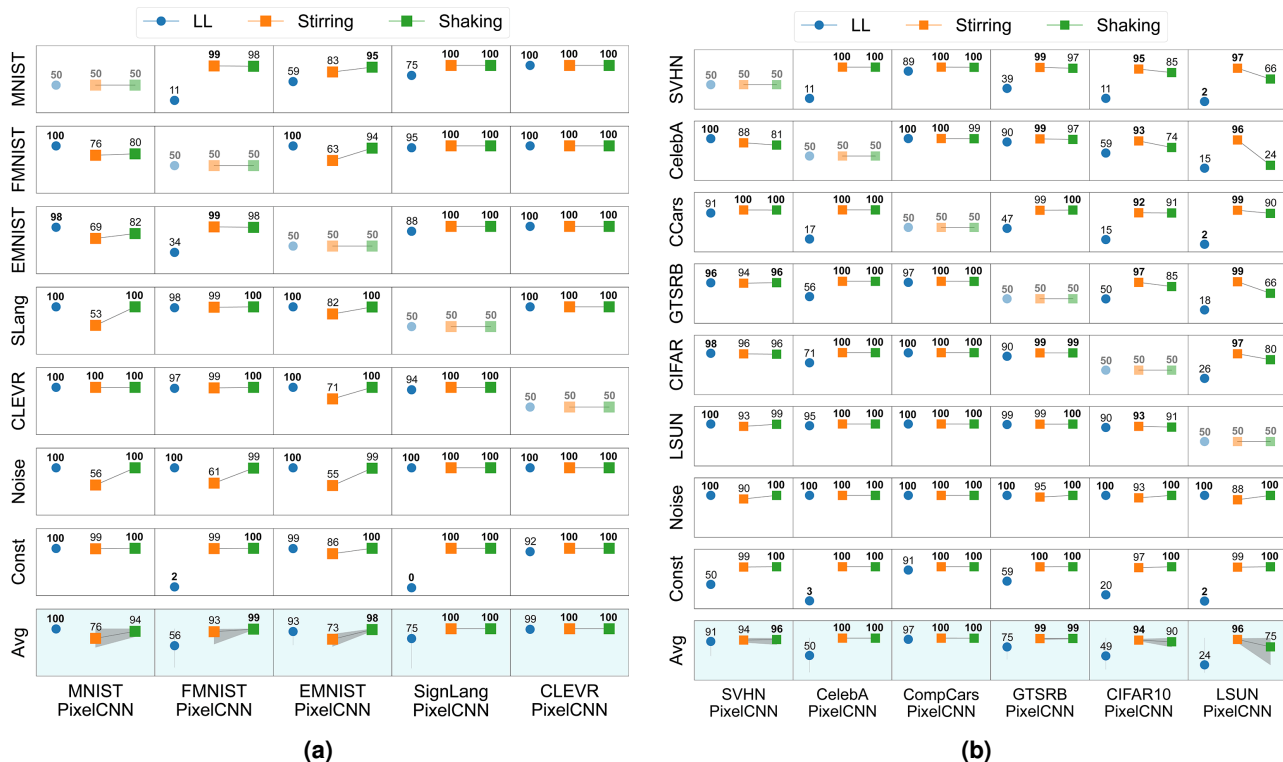


Figure 15. Outlier detection AUROC without conditional correction. (a) Grayscale image datasets. Blue: log likelihood (LL), uncorrected; Orange: Stirred LL without conditional correction; Green: Shaken LL without conditional correction. (b) Same as in panel (a) but for natural image datasets. Other conventions are the same as in Figures 5-6.

Stirring (Fig. 15a, orange symbols) and shaking (Fig. 15a, green symbols) offer improvements over log likelihood (Fig. 15a, blue symbols) in several cases while also failing in some. In particular, stirring consistently fails with Noise/OOD achieving AUROCs as low as 55%. As pointed out in Appendix. C.5, Noise/OOD is a particularly challenging for a likelihood ratio as the likelihoods assigned to Noise/OOD images are very small numbers.

For natural images, stirring (Fig. 15b, orange symbols) and shaking (Fig. 15b, green symbols) exceptionally better than log likelihood (Fig. 15b, blue symbols) even with Noise/OOD, in which case the AUROC drops to a minimum of 88% with stirring. In summary, stirring and shaking enable robust outlier detection in several cases on their own, while conditional correction ameliorates challenges with likelihood ratio to improve performance in most failure cases.

G. Alternative Approaches to “Shaking”

G.1 Varying patch sizes

In the main text, we considered some simple approaches to “shaking”, which involves splitting the image into halves or quarters and shuffling the split patches spatially. However, there are several other ways in which shaking can be performed. We describe and test few other methods of shaking for outlier detection.

So far, we have only considered splitting the image into equal halves along the horizontal or vertical mid-lines. It is

also possible to divide the image into finer, segments – either horizontally or vertically.

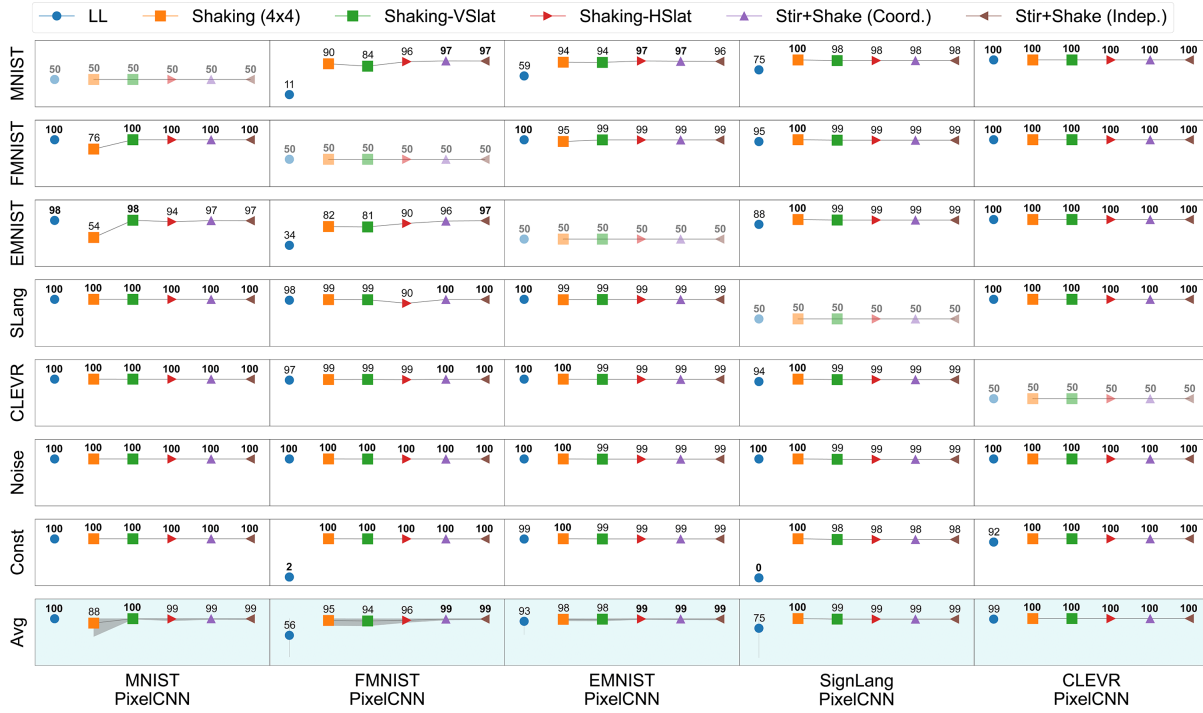
First, we split the images into four equally-sized vertical “slats”. Each slat is of size 8×32 pixels, which are then randomly shuffled around vertically, in a coordinated manner across all 3 channels. Second, we split the image into four equally-sized horizontal slats: four patches of size 32×8 pixels. In each case, 9 derangements are possible, and we summed the change in log likelihoods across the respective derangements to compute the final outlier detection score (VSlat and HSlat, respectively).

Lastly, we perform shaking with a finer grained division of image into 16 patches (4×4). In this case, each patch is of size 8×8 pixels. Because many derangements are possible with 16 patches, we randomly selected 20 derangements, and the final score was computed as the summed change in the log likelihoods across these 20 derangements.

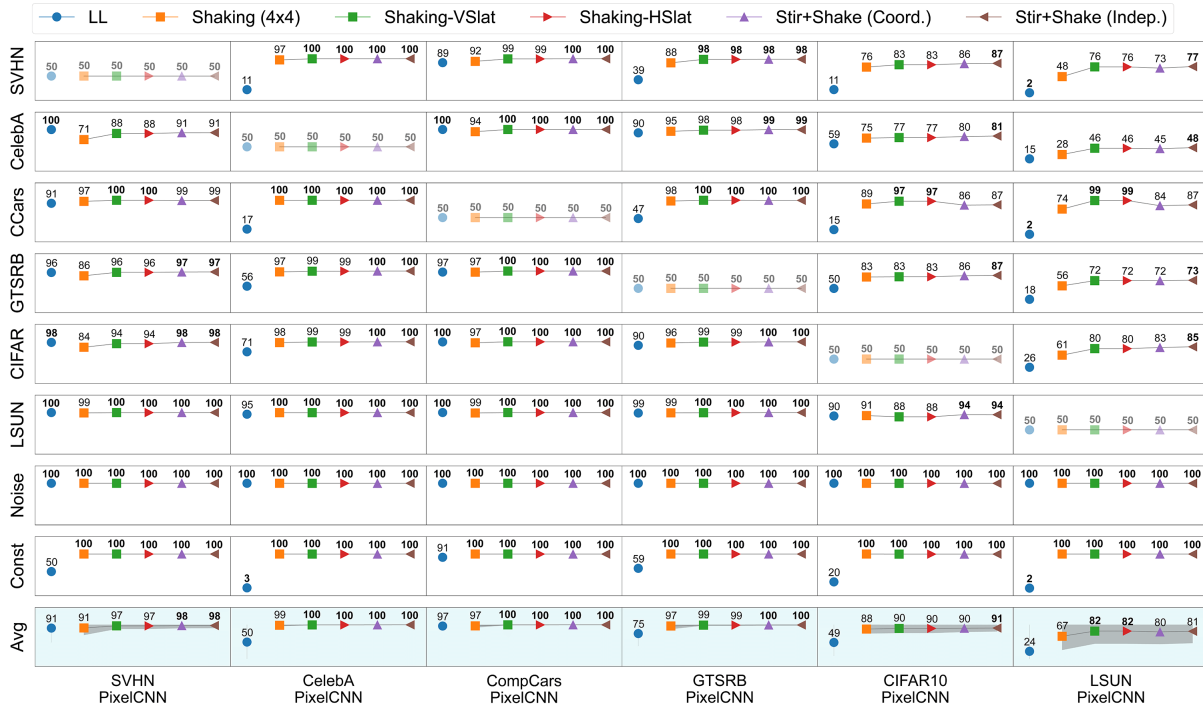
We show the outlier detection performance (AUROC) based on these alternative shaking techniques in Figure 16a for grayscale images and in Figure 16b for natural images (orange, green, and red symbols). We see that bigger patch sizes typically show better outlier detection scores (e.g. compare VSlat and HSlat with 4×4).

G.2 Combining shaking and stirring

We also considered combining shaking and stirring, to achieve a potentially greater disruption of long-range dependencies. We attempted two, among the many different ways to combine



(a)



(b)

Figure 16. Outlier detection AUROC with alternative approaches for shaking. (a) Grayscale image datasets. Blue: log likelihood (LL), uncorrected; Orange: Shaken LL with 16 patches; Green: Shaken LL with vertical slats; Red: Shaken LL with horizontal slats; Purple: Combination of Shaking and Stirring with coordinated rotation of patches; Brown: Combination of Shaking and Stirring with independent rotation of patches. (b) Same as in panel (a), but for natural image datasets. Other conventions are the same as in Figures 5-6.

the two approaches.

First, we consider coordinated rotation of all patches in the

image followed by shuffling. We split the image into four quarters of 16×16 pixels each, along the vertical and horizontal

mid-lines. We then applied the same rotational transformation to all the patches in a coordinated manner, followed by spatial shuffling. Here, a total of 63 permutations are possible (7 stirring transformations \times 9 shaking derangements). The outlier detection score was computed as the summed change in the log likelihoods across 20 randomly selected derangements.

Next, we consider independent rotation of each patch in the image followed by shuffling. Here also we split the into four quarters of 16×16 pixels, but applied independent rotations to each patch, followed by spatial shuffling. As before, the outlier detection score was computed as the summed change in the log likelihoods across 20 randomly selected derangements.

The outlier detection performance (AUROC) of these combinations of shaking and stirring is shown in Figure 16a for grayscale images and in Figure 16b for natural images (purple and brown symbols). We did not observe evidence for significant improvement in outlier detection by combining shaking with stirring (compare with Figs. 5 and 6, main text).

H. Stirring: Subpar performance with EMNIST/MNIST

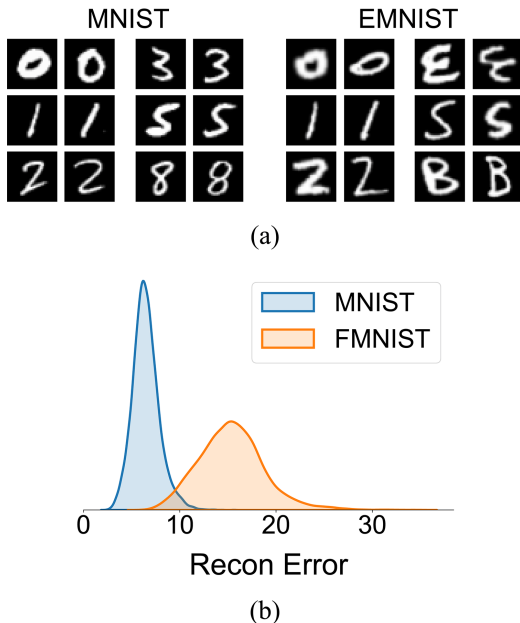


Figure 17. (a) Exemplanters from the MNIST and the EMNIST datasets illustrating the similarity of features in the images across the two datasets. (b) Reconstruction error for MNIST/OOD samples (blue) and FMNIST/OOD samples (orange) for a PixelCNN++ trained on the EMNIST dataset.

Across the 72 ID/OOD comparisons, including both grayscale and natural image datasets, stirring outlier detection performance deviated significantly from ceiling for only one case: EMNIST ID versus MNIST OOD. We analyze this case in more detail here.

MNIST is a collection of hand-written numbers, and the subset of EMNIST that we used (EMNIST-letters) is a collec-

tion of hand-written English alphabets. In both these datasets, the foreground information occurs at high intensities (almost white) and the background consists primarily of low intensity (almost black) pixels. As a result both of these datasets comprise near-binary images. We show some exemplars of both the datasets in Figure 17a. It is readily observed that there are many visually similar counterparts across MNIST and EMNIST images. For example, images of 0 and O, 1 and I, 2 and Z, 3 and E, 5 and S, 8 and B look very similar as shown in Figure 17a. We hypothesize that, as a result of this similarity, the PixelCNN++ model trained on EMNIST was powerful enough to reconstruct MNIST test images well; this yielded potential outlier detection performance. Confirming this, the reconstruction error of MNIST/OOD test samples (Fig. 17b, blue density) is substantially lower than that of the FMNIST/OOD test samples (Fig. 17b, orange density) for the EMNIST PixelCNN++.

I. Shaking: Subpar performance with CIFAR10/LSUN

Across all ID/OOD comparisons, we found that shaking performed comparably with stirring, by and large, in terms of outlier detection AUROC. Yet, shaking was noticeably worse than stirring particularly with more complex natural image datasets like CIFAR10 and LSUN. We speculate on the reasons here.

Unlike other datasets like SVHN, CelebA, CompCars or GTSRB, CIFAR10 and LSUN are, arguably, more complicated datasets, for two reasons. First, these datasets are more diverse: for example, CIFAR10 comprises images of various, unrelated categories, both animate (e.g., cats, deer, frogs) and inanimate (e.g., airplanes, cars, ships). Similarly, the LSUN (classroom) dataset comprises photographs of classrooms with diverse objects including chairs, desks, chalkboards, and people. Second, images in these datasets (even within a single class) are more heterogeneous, in that key, foreground objects occur at inconsistent spatial positions relative to the frame of the image. For both of these reasons, when split into patches across the mid-line, the likelihood that the split occurs inconsistently across key foreground objects is much higher in the more heterogeneous and diverse datasets. Consequently, across different images it may be challenging to disrupt long-range dependencies uniformly, while preserving local dependencies, in these datasets. We speculate that this is the primary reason for the weaker performance of shaking (as compared to shuffling) with these datasets.

This reasoning suggests that shaking with smaller patch sizes should yield progressively worse outlier detection performance with these (CIFAR10 and LSUN) datasets, given that smaller patches would increase the chances of more inconsistent splits of foreground objects. Providing tentative validation to this hypothesis, smaller patches sizes yielded substantially worse AUROCs (upto $\sim 15\%$) especially for the LSUN dataset (Fig. 16b, small 4×4 patches, orange symbols versus larger slats, green and red symbols).

J. Reproducibility Checklist

Data: All datasets used in this study are publicly available, and data sources are provided in Appendix B.

Experimental results:

- Evaluation metrics (AUROC, AUPRC, FPR@80%TPR) are standard outlier detection metrics in literature, and described in Appendix D.
- Train/test/validation splits are detailed in Appendix B and selection of hyperparameters of “tf.distributions.PixelCNN” to replicate our model architecture are shown in Table. 1.
- The default shuffling order of the test sets from their respective sources were used. For generating Noise and Constant OOD samples, NumPy⁶ 1.19.5 was used with a random seed of 42. The first 5000 test images were used for computing outlier detection performance.
- TensorFlow 2.6.0 was used to train the models, and its random seed was set to 42 to initialize the PixelCNN++ networks.

Code:

- We have described, in full detail, the implementation of the $\log p_{LR}$ with stirring and shaking introduced in this study (Section 3.5) for reproducibility.
- We have also specified in detail all the relevant software libraries and frameworks used in appropriate places (Appendices A, B, D).
- Code for reproducing the results will be made publicly available after paper acceptance.

Compute Environment: All experiments were performed on local systems equipped with two NVIDIA GTX 1080Ti GPUs and 64GB of memory.

⁶<https://numpy.org/>